



Ce-modified zeolite BEA catalysts for the trichloroethylene oxidation. The role of the different and necessary active sites

Kinga Gołabek^a, Antonio E. Palomares^b, Joaquín Martínez-Triguero^{b,*}, Karolina A. Tarach^a, Krzysztof Kruczała^a, Vladimir Girman^c, Kinga Góra-Marek^{a,*}

^a Faculty of Chemistry, Jagiellonian University in Kraków, 2 Gronostajowa St., 30-387 Kraków, Poland

^b Instituto de Tecnología Química, Universitat Politècnica de València-CSIC, Camino de Vera s.n., 46022 Valencia, Spain

^c Pavol Jozef Šafárik, University in Košice, Department of Condensed Matter Physics, Park Angelinum 9, 041 54 Košice, Slovakia



ARTICLE INFO

Keywords:

Cerium
Zeolites
Acidic properties
Oxidation of trichloroethylene
Superoxide radicals

ABSTRACT

This paper reports the activity of different Ce-BEA zeolites for the catalytic oxidation of trichloroethylene and it is focused on determining the nature of the catalyst active sites. The study was made by using a microporous zeolite BEA, two types of desilicated BEA zeolites and mildly steamed desilicated BEA zeolites. The catalysts were prepared by introducing Ce to the zeolites with incipient wetness impregnation and their structural, textural, and acidic properties were established. The evolution of TCE conversion was correlated with the physicochemical properties of the zeolites. It is shown that highly developed mesopore surface area, well-dispersed cerium species and a high number of Brønsted sites results in the highest activity. The activity and selectivity of the Ce-loaded zeolites were found to be dependent on the number of high strength Brønsted acid centres. The hierarchical materials with a higher density of hydroxyls showed higher yields to HCl while the formation of chlorine was prevented.

1. Introduction

Industrialization, while important for the economic growth and development of a society has a major impact on the natural environment. Chlorinated hydrocarbons (Cl-VOCs), belonging to the group of volatile organic compounds (VOCs), have gained acceptance as chemical solvents and intermediates in the polymer industry but the harmful effects of VOCs emissions have led to new environmental legislation [1].

Thermal incineration is a commonly used method for the treatment of streams containing a high concentration of volatile organic compounds. The main disadvantage of this approach, from the economical point of view, is the high cost of exploitation e.g. to achieve complete trichloroethylene (TCE) destruction, temperatures exceeding 800–1200 °C are required. Simultaneously, other disadvantages from the environmental point of view are the poorly controlled emissions of undesirable by-products, dangerous for human health [2,3]. Some alternative technologies have been proposed e.g. low-temperature condensation [4], biochemical methods [5], adsorption-based techniques [6] and catalytic combustion [7]. The last one is the most interesting from the economic and environmental point of view as it uses low temperatures and does not transfer the pollutants to another phase as in

condensation or adsorption technologies.

Different catalysts as alumina supported noble metal have been deeply investigated in terms of destructive oxidation of Cl-VOCs [8]. It has been described that the use of platinum and palladium as active phases results in active and selective catalysts at low temperatures, however, their industrial application is limited because of the cost and sensitivity of the noble metal catalysts that can be easily poisoned [9,10]. Thus, non-noble metal catalysts such as Cu/Mg/Al hydrotalcites [11,12], Mo and/or W-based bronzes [13], Co/Ni-Fe-Al mixed oxide [14], Mn-doped ZrO₂ [7], V₂O₅-WO₃/TiO₂ [15] or mayenite materials [16], become low cost alternatives offering improved activity and resistance to poisoning. Zeolites have also gained interest as potential active catalysts in Cl-VOCs oxidation [17,18] because of their high surface area, adsorption capacity and thermal stability. Recent literature reports have revealed the potential of H-zeolites as an effective alternative to noble and metal oxide catalysts used in most commercial applications for VOCs removal [19,20]. G.A. Atwood et al. [17] have shown that at room temperatures acid sites located in ZSM-5 facilitate TCE adsorption resulting in an improved oxidative activity. Kosusko et al. [3] have established a relationship between the catalytic activity for VOC destruction and the adsorption capacity of reactants over zeolites. Addition of metals to the zeolite results in an improved redox

* Corresponding authors.

E-mail addresses: jomarti@itq.upv.es (J. Martínez-Triguero), kinga.gora-marek@uj.edu.pl (K. Góra-Marek).

activity as it was described in a recent review by Gonzalez-Velasco et al. [21]. Cobalt on BEA zeolite [22] show interesting results but there are some concerns about the toxicity of this metal. Copper exchanged zeolites have been also used [22,23] for this reaction and good results have been obtained. Other transition metals can be also interesting for this reaction. Cerium oxide is a well-known material with improved redox properties and with oxygen storage ability. The CeO₂/ZSM-5 catalyst was tested for the oxidation of other chlorinated compounds [24], then this metal is a potential candidate for its use in the TCE oxidation reaction.

The catalytic activity of cerium oxide is linked with the ability to undergo a redox reaction. This in turn enables Ce-based catalysts to mimic analogous behaviour of noble metals [25]. Therefore, the Ce-based materials serve as an oxygen buffer in prominent chemical reactions, most notably water-gas shift reactions, hydrocarbon oxidation [26], NO_x conversion into nitrogen [27,28], and oxidation of chlorinated volatile organic compounds. A plausible reaction mechanism of TCE catalytic combustion over CeO₂ catalysts assumes the formation of a very reactive chloroacetylene (C₂HCl) intermediate. At short sufficiently residence times C₂HCl undergoes decomposition to HCl/Cl₂ and CO₂/CO whereas at prolonged residence times the formation of tri- and hexachlorobenzenes has been reported [29]. Ceria may therefore play a dual role in the destruction of aromatic pollutants as it strongly fixes radicals mediating formation of dioxin-type compounds [30,31].

In the total TCE oxidation relatively non-hazardous compounds such as carbon dioxide, water, and hydrochloric acid are obtained. However, it is well known that Al-O bonds in the zeolite framework can be easily attacked by the HCl formed, leading to the formation of volatile AlCl₃. Extraction of Al atoms causes an intense drop in the acidic properties as well as clogging of micropores or even a partial collapse of the zeolite framework [32–34]. The type of zeolite structure, the Si/Al ratio, the number of Brønsted acid sites, the crystal size or the number of defect sites are factors affecting the demetalation processes of a zeolite [35] and this is strongly enhanced by the presence of water and HCl. Then, the modification of the pore hierarchy in the zeolite through the production of secondary mesoporosity, by a caustic treatment, may favour a fast diffusion of both HCl and water molecules preventing the Al-sites from extraction. Besides, the presence of intracrystalline mesoporosity can also alter the speciation of both redox and acid sites in the zeolite. For instance, Al atoms reinserted [36] in the zeolite framework during alkaline treatment were found to form protonic sites of the nature similar to the protonic sites in amorphous aluminosilicates. Those protonic sites have shown lower resistance toward dehydroxylation than typically zeolitic Si(OH)Al bridging hydroxyls [37–39]. What is more, aluminium centres located on the mesopores surface can react with molecules containing Cl.

In this work, we attempted to answer the question whether the nature of acidic sites influences the oxidation of trichloroethylene by changing the acidic properties of the microporous zeolites with caustic and thermal treatments. Such procedure provoked the transformation of the Si(OH)Al bridging hydroxyls into both Lewis as well as new Brønsted acid sites, typical of mesoporous amorphous materials. The catalytic parameters of the materials obtained were discussed in terms of acid sites, pore hierarchy, and cerium dispersion. In addition we have studied the influence of the Lewis and Bronsted acidity of the support by comparing the catalytic activity of the Ce-BEA zeolite with that of Ce-supported on silica and alumina catalysts.

2. Materials and methods

2.1. Catalysts preparation

A commercial microporous ammonium beta zeolite of Si/Al = 19 (CP814C supplied from Zeolyst Corp.) denoted as H-β was used as parent material. The mesoporous materials were prepared from the parent zeolite by a caustic treatment. It was performed with a 0.2 M

solution of NaOH or with a 0.2 M solution containing a mixture of NaOH and TBAOH with a molar ratio TBAOH/(NaOH + TBAOH) of 0.4 (samples denoted as H-β^N and H-β^T, respectively). 100 cm³ of the solution was added to 3.0 g of zeolite and stirred at 65°C for 15 min. After that the suspension was cooled down in an ice-bath, filtered and washed until neutral pH. Subsequently, Na⁺/NH₄⁺ ion-exchange was carried out using a 0.5 M solution of NH₄NO₃ at 65°C for 1 h. Finally, the zeolites were again filtered, washed with distillate water and dried overnight at room temperature. All the zeolites were calcined at 450°C for 7 h to be transferred in their protonic forms. Mildly steamed materials, hereafter denoted with 550 as a subscript, were obtained by the calcination at 550°C in the presence of water vapour in static conditions. γ-Alumina (Pural from Sasol) and silica (Aldrich) were also used as supports for the cerium oxide.

The incorporation of the cerium to all the samples was realized by incipient wetness impregnation. The dry support was impregnated with an aqueous solution of cerium nitrate hexahydrate (Ce (NO₃)₃·6H₂O > 99% from Merck). The nominal mass loading of cerium was 2% wt. for all catalysts. To achieve incipient wetness a liquid/solid ratio of 1.12 cm³ g⁻¹ was used. After impregnation, the samples were dried overnight at room temperature and calcined at 450 °C for 7 h in air atmosphere.

2.2. Catalyst characterization

The textural parameters of the catalysts were obtained by liquid nitrogen sorption (−196 °C) measurements on ASAP 2420 Micromeritics after activation in vacuum at 400 °C for 12 h. Surface areas were calculated using the Brunauer, Emmet and Teller (S_{BET}) model and the de Boer “t-plot” method was applied to calculate the micropore volume (V_μ) and micropore surface area (S_μ). The external surface area was estimated as $S_{EXT} = S_{BET} - S_\mu$.

Powder X-ray diffraction patterns (XRD) were collected using a PANalytical Cubix diffractometer, with CuKα radiation, $\lambda = 1.5418 \text{ \AA}$ and a graphite monochromator in the 2θ angle range of 5–50°. The X-ray patterns were used to determine the relative crystallinity value (%Cryst) for all studied catalysts. The calculation of the relative crystallinity value was based on the integral intensity of the characteristic peaks in the range between 20° and 30°.

The chemical composition of all samples was achieved by inductively coupled plasma (ICP-OES) measurements in a Varian 715-ES ICP-Optical Emission Spectrometer. The samples were degassed under vacuum at 350 °C for 10 h prior to analysis.

The temperature-programmed reduction (TPR) of all the catalysts was carried out using the flow of mixture gases H₂ and He (10 vol % H₂ in He) as a reducing agent (flow rate = 40 cm³ min⁻¹). A sample (20 mg) in the form of powder was packed in a quartz tube ($\varnothing = 5 \text{ mm}$), treated in a flow of helium at 250 °C for 2 h, then in oxygen flow for 1 h at the same temperature and cooled to room temperature (RT). Then the catalyst was heated at a rate of 5 °C min⁻¹ to 800 °C in the presence of the reducing mixture. Hydrogen consumption was measured by a thermal conductivity (TCD) detector.

The high-resolution TEM micrographs were obtained using transmission electron microscope (JEOL 2100 F UHR) working at 200 KV, with Field Emission Gun (FEG). The sample was suspended in ethanol and sonicated for 5 min. A drop was deposited onto a copper grid coated with an ultrathin layer of carbon until dryness.

FTIR study of the samples was made using self-supporting wafers (ca. 5–10 mg cm⁻²). Prior to the study, the materials were pre-treated in situ in the quartz IR cell at 450 °C or 500 °C under vacuum conditions for 1 h. The IR spectra were recorded with a Vertex 70 spectrometer equipped with an MCT detector. The spectral resolution was 2 cm⁻¹. The concentration of Brønsted and Lewis acid sites was determined by quantitative IR adsorption studies of pyridine (Avantor Performance Materials Poland S.A.). The sample was saturated with pyridine vapour at 170 °C and next evacuated at the same temperature to remove the

gaseous and physisorbed pyridine molecules (Py). Then, the IR spectrum was taken at the same temperature. The concentration of Brønsted and Lewis sites was calculated using respectively the intensities of the 1545 cm^{-1} band of the pyridinium ions PyH^+ and the 1455 cm^{-1} band of pyridine coordinatively bonded to Lewis sites (PyL). The values of the extinction coefficient were $0.07\text{ cm}^2\text{ }\mu\text{mol}^{-1}$ for the PyH^+ band and $0.10\text{ cm}^2\text{ }\mu\text{mol}^{-1}$ for the PyL band [38].

The acid strength was determined based on Py thermodesorption studies. The conservation of the 1545 cm^{-1} band of the PyH^+ ions band and the 1455 cm^{-1} band of pyridine coordinatively bonded to Lewis sites under the desorption procedure at 450°C , expressed as $\text{Py}_{450}/\text{Py}_{170}$ ratio, was taken as a measure of the acid strength.

The micro-Raman analysis was performed with a Renishaw InVia dispersive spectrometer equipped with a CCD detector and integrated with a Leica DMLM confocal microscope. An excitation wavelength of 514.5 nm was provided by an Ar-ion laser (Spectra-Physics, model 2025). The spectra were recorded at ambient conditions with the resolution of 2 cm^{-1} . The Raman scattered light was collected with a 50 Olympus objective in the spectral range of $1000\text{--}2000\text{ cm}^{-1}$. The same number of accumulations were taken from three different points of the surface of each catalyst and then averaged.

CW-EPR spectra were recorded using Bruker X-band ELEXSYS E500 spectrometer operating at 9.7 GHz and 100 kHz magnetic field modulation. A microwave power of 2 mW , modulation amplitude of 0.1 mT , a conversion time of 81.92 ms , a time constant of 40.96 and 16 scans were applied in the measurements. The samples were measured without prior activation, after degassing for 30 min at room temperature and after activation at 450°C under vacuum. In the next step adsorption of 50 Torrs of oxygen at 450°C was performed. After 20 min , the samples were outgassed for 1 min at the same temperature. Spectra of all samples were recorded at ambient and liquid nitrogen temperatures (-196°C). In order to determine the EPR parameters of the paramagnetic species, a simulation procedure (EPRSIM32) was used [40].

2.3. Catalyst activity tests

Prior to the catalytic tests, all the catalysts were pelletized, then crushed and sieved to obtain grains of $0.25\text{--}0.45\text{ mm}$ diameter. The catalytic tests have been performed in a quartz fixed bed reactor. The desired mass of the catalyst (0.68 g) was placed on a quartz plug located inside the reactor. Crushed quartz was placed above the catalyst as a preheating zone. The temperature was measured with a K-thermocouple located inside the reactor and the reactor was heated using an electric oven. The flow rate was set at $400\text{ cm}^3\text{ min}^{-1}$ and the gas hourly space velocity (GHSV) was $15,000\text{ h}^{-1}$ at atmospheric pressure. The residence time, based on the packing volume of the catalyst, was 0.24 s . Liquid trichloroethylene was injected in air flow with a syringe pump in order to have 1000 ppm of TCE in the gas flow. The reaction temperature was increased from 150 to 550°C in steps of 50°C . The catalysts were kept at each temperature for 30 min before the analysis of the gaseous products. The overall length of the reaction was 6 h . The organic compounds present in the gas flow were analyzed with a Bruker 450 gas chromatograph equipped with an HP-5 column and with a flame ionization detector. CO and CO_2 were separated with micro-packed columns and analyzed with a thermal conductivity detector. The chlorine products, i.e. Cl_2 and HCl were absorbed in a solution containing NaOH 0.0125 M . The concentration of the absorbed Cl_2 was determined by titration and the HCl concentration was measured using an ion selective electrode. All the experiments were repeated three times to assure the reproducibility of the results. In all the experiments the error analysis of triplicate results was under 5% . Calculation of conversions and selectivities is described elsewhere. [11]

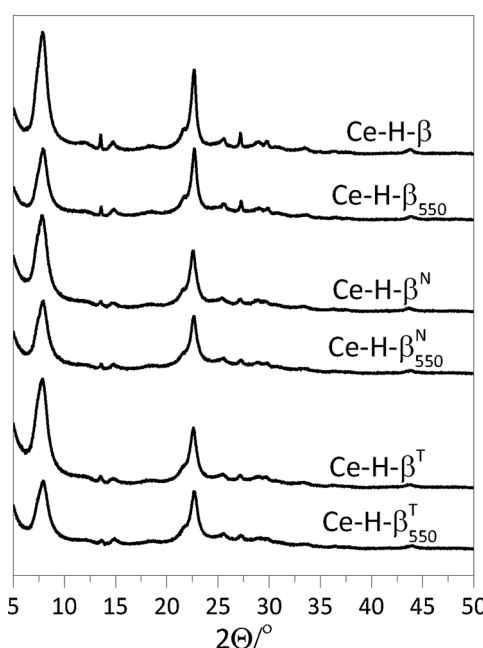


Fig. 1. XRD patterns of Ce-modified materials.

3. Results and discussion

3.1. Structural and textural characterization

XRD patterns of cerium-containing zeolites show the presence of the characteristic peaks of BEA zeolites with peak intensities similar to those of the native supports confirming the stability of catalysts prepared (Fig. 1). However, some loss of crystallinity is noticed (% Cryst., Table 1) due to the generation of secondary mesoporosity. No amorphous material was detected and no peaks associated to cerium oxides were observed, indicating that cerium particles are beyond the detection limit of the X-ray diffraction due to good dispersion of cerium oxide species on the catalyst surface and/or to their amorphous nature [41] and low content.

The textural analysis was carried out by N_2 physisorption (Table 1). The surface area of the parent zeolite increases after the caustic treatments due to the increase of the mesopore surface area ($52\text{--}377\text{ m}^2\text{ g}^{-1}$). This is typical for zeolites with highly developed secondary mesoporosity. The generation of mesopore system only marginally influences the microporous environment, what is reflected in the maintaining or the negligible decrease of the V_μ values. Calcination at 550°C slightly changed the micropore volume and surface area of the parent zeolite H- β , whereas obvious alteration of V_μ parameters of desilicated zeolites H- β_{550}^N and H- β_{550}^T is indicative for their lower thermal resistance than parent counterpart. The external surface area (S_{EXT}) values are higher for mildly steamed desilicated zeolites H- β_{550}^N and H- β_{550}^T than for non-treated analogues.

The cerium deposition affects the micropore volume and area values for all the materials studied. The observed changes are representative for the preferential accommodation of cerium species in micropores. The Ce-doped hierarchical zeolites seem to possess lower thermal stability. Calcination at 550°C leads to a significant drop of micropore volume, in exception of Ce-H- β^N . The textural properties of alumina and silica are also affected by cerium moieties resulting in the reduction of surface area and pore volume.

The generation of secondary mesoporosity is clearly observed by transmission electron microscopy (HAADF-STEM). The crystallites of mesoporous zeolites are around 350 nm and identical to the parent zeolite BEA. The incipient wetness impregnation procedure did not modify the overall appearance of the zeolite at a microscopic level. In

Table 1

The composition of the zeolites determined by chemical analysis (Si/Al), the % of crystallinity calculated from XRD patterns and textural parameters from low-temperature N₂ adsorption for the materials studied.

Zeolite	Si/Al _{ICP}	% Cryst.	S _{BET} [m ² ·g ⁻¹]	S _{EXT} [m ² ·g ⁻¹]	S _μ [m ² ·g ⁻¹]	V _μ [cm ³ ·g ⁻¹]
H-β	19	100	724	52	672	0.28
Ce-H-β		91	675	47	629	0.26
H-β ₅₅₀		100	740	80	660	0.27
Ce-H-β ₅₅₀		89	578	64	514	0.21
H-β ^N	12	91	915	366	528	0.26
Ce-H-β ^N		85	838	468	370	0.18
H-β ₅₅₀ ^N		90	848	377	482	0.23
Ce-H-β ₅₅₀ ^N		82	715	341	374	0.18
H-β ^T		89	843	236	606	0.30
Ce-H-β ^T		85	882	303	579	0.29
H-β ₅₅₀ ^T		87	892	384	508	0.24
Ce-H-β ₅₅₀ ^T		81	804	409	395	0.20
γ-Al ₂ O ₃	—	—	265	—	—	V _{pore} [cm ³ g ⁻¹]
Ce-γ-Al ₂ O ₃		—	222	—	—	0.39
SiO ₂		—	460	—	—	0.30
Ce-SiO ₂		—	411	—	—	0.55
						0.42

HAADF-STEM micrographics, the particles of cerium oxide can be easily observed only for Ce-SiO₂ (Fig. 2). In the zeolites mildly steamed at 550 °C, cerium particles with higher crystallite size can be distinguished (1–5 nm) suggesting the location of those moieties on the mesopore surfaces. For the zeolites Ce-H-β, Ce-H-β^N, and Ce-H-β^T the effortfully detected cerium particles of the 1.5 nm evidence their very high dispersion within micropore structure. The micropore environment favors the formation of the smallest cerium species, still however in mesoporous materials Ce-species evidence only slightly lower stability against sintering in comparison with microporous analogues [42,43]. Higher crystallite size of cerium species over silica and alumina can be related to the lower specific surface area of both supports.

The reducibility of all the catalysts was studied by H₂-TPR, and the corresponding TPR profiles are shown in Fig. 3. For ceria, chosen as a reference system, the first hydrogen consumption peak visible in the temperature range of 330–580 °C is connected with the reduction of CeO₂ surface species to non-stoichiometric oxides CeO_{2-x}. The high-temperature peaks located above 670 °C come from the bulk CeO₂ reduction [44]. The H₂-TPR profile of the Ce-modified alumina exhibits a reduction profile shifted to the lower temperatures than this observed for pure ceria [45]. This tendency becomes more dominant for Ce-zeolites, both low-temperature and high-temperature reduction peaks are significantly shifted to lower temperatures (ca. 50 °C). Furthermore, the high-temperature peak significantly diminishes, evidencing more effective surface reduction than bulk reduction [45]. The similar reducible behaviour of all the zeolite-based catalysts compared to ceria points to the presence of highly dispersed cerium oxide-like species, as manifested by TEM micrographs (Fig. 2). The ability of the Ce⁴⁺ to undergo a facile redox reaction is the foremost reason for the increase of the surface-oxygen-vacancies. With respect to CeO₂, an increment (ca. 20%) in the profile area can also be observed for Ce-H-β and Ce-H-β^T which is associated with higher H₂ consumption and the achievement of higher reduction percentage of Ce⁴⁺ moieties accommodated in these zeolites.

3.2. Spectroscopic characterization

3.2.1. IR studies of O–H region

The region of stretching O–H vibrations is presented in Fig.SI.1. The enhanced population of isolated silanols (Si–OH_{iso}), represented by the 3745 cm⁻¹ band, can be attributed to the external area development due to the mesoporosity fabrication. Also, the formation of hydrogen-bonded silanols as internal defects is easily detected for mildly steamed H-β₅₅₀. The lower Si/Al ratio in desilicated materials

compared with the parent zeolite indicates an increased number of Al atoms in hierarchical materials. On the other hand, the band of the bridging Si(OH)Al hydroxyls groups (3605 cm⁻¹) did not rise in intensity suggesting that the Al sites reinserted during desilication do not provide the bridging zeolitic Si(OH)Al sites. While the cerium species are deposited, the partial consumption of the Si(OH)Al band is observed due to the effective neutralization of the negative charge of zeolite framework by one or two positively charged complex cerium hydroxyls [46]. The involvement of the Si – OH groups in the interaction with cerium species can be also concluded, as manifested by the reduced number of silanols in Ce-zeolites. The erosion of the 3605 cm⁻¹ bands in the mildly steamed hierarchical zeolites provides an argument for the sensitivity of bridging Si(OH)Al hydroxyls to thermal treatment [37,39,47]. The species that survived high-temperature treatment are hardly detectable in the IR spectrum as the Si(OH)Al band, the most probably due to the low value of the absorption coefficient [39]. The Ce-SiO₂ consists mainly of large separate domains of the two oxides, as evidenced by TEM images. Indeed, no consumption of silanols is observed after cerium deposition on silica: the 3745 cm⁻¹ band in SiO₂ and Ce-SiO₂ materials are of the same intensity. In contrast, for alumina support, the intensive development of 3732 and 3580 cm⁻¹ bands is representative for the formation of cerium oxyhydroxide microphases located on the alumina surface [48]. The 3674 cm⁻¹ band characteristic of OH groups associated with Ce³⁺ species [49] is not distinguishable in the zeolitic catalysts.

3.2.2. IR quantitative Py adsorption

The concentration of Brønsted acid sites was quantitatively determined in the pyridine sorption experiments (PyH⁺ in Fig.SI. 2, Table 2). The highest number of Brønsted sites was found for the purely microporous H-β, i.e. the material with the lowest Al content. The alkaline-treated materials H-β^N and H-β^T are enriched in Lewis acid sites, the most probably due to higher susceptibility of protonic sites to dehydroxylation. Indeed, independently from the pore hierarchy, the calcination at 550 °C provokes the transformation of Brønsted sites into Lewis acid entities. The differentiated nature of Lewis acid sites is clearly seen in the spectra of Py adsorbed. The Lewis species of the highest strength, thus represented by a higher frequency of PyL adduct band (ca. 1453 cm⁻¹) are present in the H-β. The generation of additional mesoporosity does not affect the Lewis sites nature and the electron acceptor sites are represented by the 1454 cm⁻¹ band typical of the microporous material. However, the emergence of the new type of Lewis acid sites of lower strength (the PyL band at 1444 cm⁻¹) can be recognized as a result of the introduction of cerium species. When

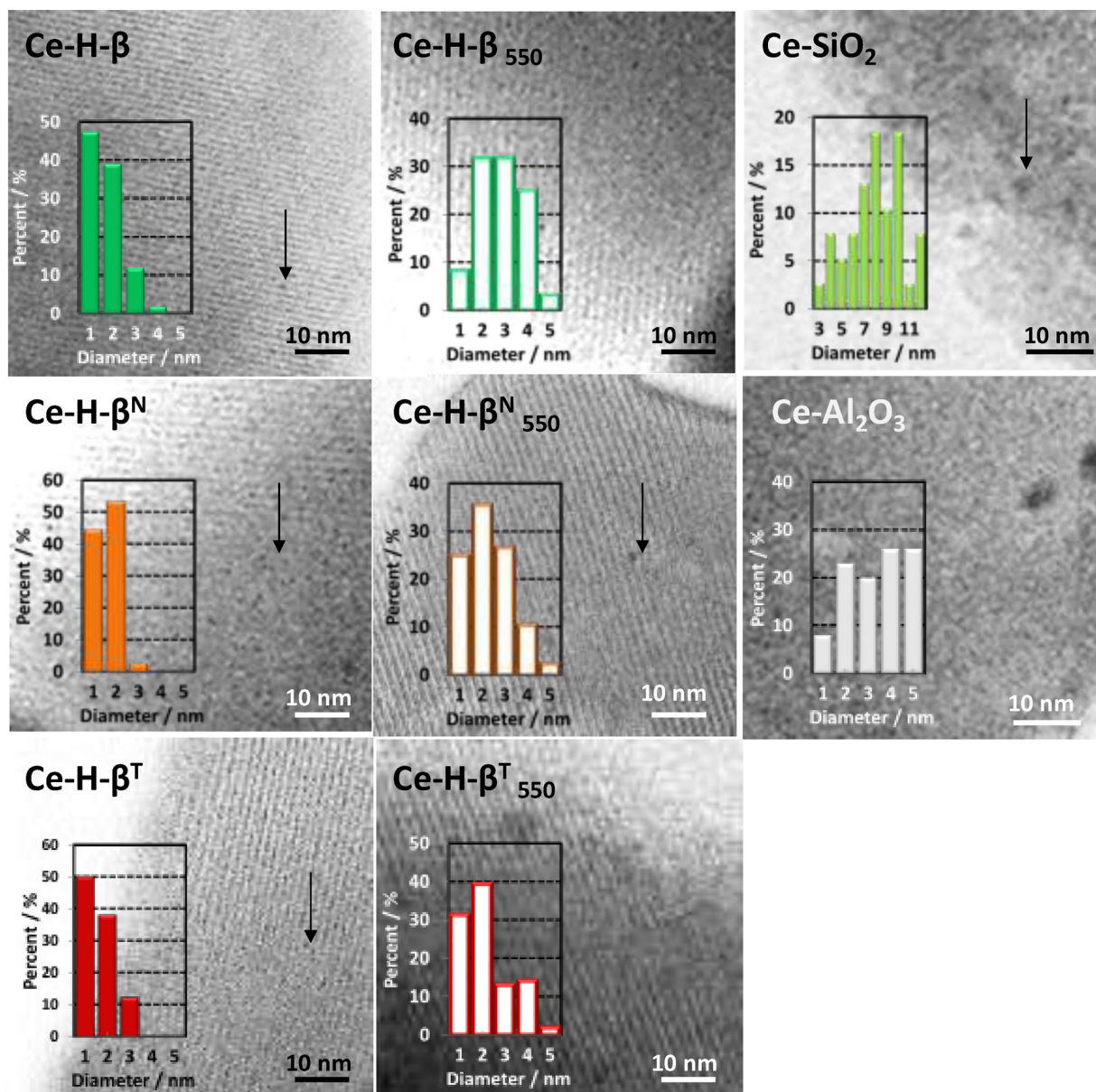


Fig. 2. TEM micrographs (the Ce-particles are pointed by arrows).

considering acidic characteristics of alumina and silica supports it can be anticipated that an additional number of Lewis sites appeared after the Ce deposition.

The strength of the protonic sites was calculated as the ratio between the PyH^+ band for the material treated at 450°C to that at 170°C (Table 2). The strength of protonic sites decreases after mesoporosity fabrication. The Si(OH)Al hydroxyls in mesoporous materials are very prone to dehydroxylation thus the thermal treatment (calcination at 450°C) at relatively low temperatures impose their transformation to Lewis sites. This effect is even more evident at a higher temperature (mild steaming at 550°C) when the bridging Si(OH)Al hydroxyls band (3605 cm^{-1}) is totally erased. It is worth noticing that the materials $\text{H-}\beta_{550}$, $\text{H-}\beta_{550}^N$, and $\text{H-}\beta_{550}^T$ possess a high amount of protonic sites detected with pyridine in spite of the low and even marginal intensity of the Si(OH)Al group bands (Fig.SI.1). The Brønsted acidity of protonic zeolites is due to the bridging Si(OH)Al groups formed through a covalent bond to oxygen atom bridging between a silicon and an aluminium atom. Such zeolite-like species of defined geometry can be also found in mesoporous aluminosilicates, however, in very low extent

[37,39,47]. On mesoporous surfaces, the proton delivering moieties can be formed by Al^{IV} and Al^V entities interacting with neighbouring Si-OH . Both Al^{IV} and Al^V - originated bridging hydroxyls showed comparable acidity to protonate ammonia molecules [50]. Further, in mildly steamed mesoporous zeolites the silanol groups perturbed by neighbouring electron acceptor aluminium species can also increase the protonic acidity, especially in the presence of strong bases as pyridine. Among the Ce-mesoporous zeolites, the $\text{Ce-H-}\beta^T$ provides the highest concentration of Brønsted acid sites.

The total acidity in H-zeolites was also compared per mol of Al atoms (Table 2). The sum of the concentrations of Brønsted and Lewis acid sites divided by the amount of Al in the protonic forms of zeolitic materials $(B + L)/Al$ expresses, which fraction of Al atoms is able to form either Brønsted or Lewis acid sites. For microporous zeolite $\text{H-}\beta$ 84% of all Al atoms can be detected by pyridine, suggesting that a large fraction of Al atoms are exposed on the surface giving rise to acid sites; only 16% of Al is either hidden in the bulk phase of extra-framework material. The drop of $(B + L)/Al$ value for desilicated support materials confirms the tendency of Brønsted acid sites to be

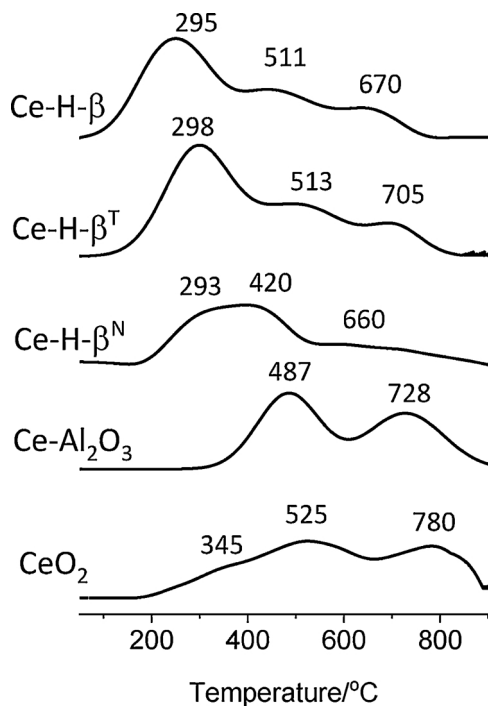


Fig. 3. TPR profiles performed for Ce-materials studied.

Table 2

The concentration of Al atoms from chemical analysis Al_{ICP} . The concentration of Brønsted (B), Lewis (L) and cerium (Ce) acid sites as well as the strength of sites A_{330}/A_{170} from IR spectroscopy measurements with pyridine.

Samples	Al_{ICP} [$\mu\text{mol}\cdot\text{g}^{-1}$]	Py [$\mu\text{mol}\cdot\text{g}^{-1}$]			(B + L)/ Al %	$\text{Py}_{450}/\text{Py}_{170}$	
		B	L	B + L		B	L
H- β	856	399	316	715	84%	0.85	0.75
Ce-H- β		364	779	1143		0.90	0.88
H- β_{550}	856	396	266	662	77%	0.90	1.00
Ce-H- β_{550}		196	566	762		0.80	0.75
H- β^N	1200	383	415	798	67%	0.70	0.70
Ce-H- β^N		295	730	1025		0.65	0.55
H- β_{550}^N	1200	267	676	943	76%	0.95	1.00
Ce-H- β_{550}^N		262	689	951		0.45	0.75
H- β^T	1200	264	424	688	57%	0.75	0.70
Ce-H- β^T		372	732	1104		0.65	0.45
H- β_{550}^T	1200	240	415	655	55%	1.00	0.95
Ce-H- β_{550}^T		262	499	761	–	0.40	0.65
$\gamma\text{-Al}_2\text{O}_3$	–	–	280	280	–	–	0.9
Ce- $\gamma\text{-Al}_2\text{O}_3$		–	353	353	–	–	0.8
SiO_2	–	–	15	15	–	–	0.0
Ce- SiO_2		–	76	76	–	–	0.0

transformed in poorly dispersed extra-framework Lewis moieties.

The Lewis acidity in the Ce-zeolites comes from their initial Al-acidity (1454 cm^{-1}) and cerium species deposited (1444 cm^{-1}). After cerium deposition, the consumption of Al-species (1454 cm^{-1}) accompanied by the rise of the Ce-species band (1444 cm^{-1}) is clearly detected in the spectra of Py adsorbed (Fig.SI. 2). It could point to the formation of Ce-... Al-O entities [46] that offer poorer electron acceptor characteristic, if any. The preferential interaction between cerium species and extra-framework Al-amorphous phase influencing the location of cerium has been reported for zeolite HUSY [49]. Further, the Ce-species highly dispersed on alumina were described as “precursors” of the Ce- $\gamma\text{-Al}_2\text{O}_3$ phase (which contains Ce^{3+}) [51,52]. The number of cerium oxide species was roughly estimated as the difference between the number of Lewis sites accommodated in H-zeolites and their Ce-counterparts. Among the zeolites studied, the Ce-H- β^T provides

a high dispersion of the cerium species (Fig. 2) and combines distinctive properties regarding highly developed mesopore surface area with preserved microporosity (Table 1) and a high number of Brønsted sites preserved (Table 2). After the mesopore system generation, the strength of Brønsted sites decreases in all the Ce-zeolites, in line with the drop of $\text{Py}_{450}/\text{Py}_{170}$ values (Table 2). The presence of the electron acceptor Ce species and/or of the Ce/Al phases justify the enhanced number of Lewis acid sites in Ce- $\gamma\text{-Al}_2\text{O}_3$. The formation of new surface compounds also offering Lewis acid sites [53] cannot be excluded also in Ce- SiO_2 .

3.2.3. On the nature of cerium-oxide species

The Raman spectroscopic investigations (Fig. 4) were carried out to identify the oxygen species present in the as made catalysts and in those treated in an oxygen atmosphere. In all the catalysts the bands characteristic to ceria moieties were not detected, except the subtle band at 460 cm^{-1} assigned to the F_{2g} mode of CeO_2 [54]. The intensity of the F_{2g} mode increases significantly for all the materials when contacting them with an oxygen atmosphere at 450°C . Both for silica and zeolitic materials the position of F_{2g} signal was found to be a red-shifted to 457 cm^{-1} and 442 cm^{-1} , respectively, compared with the position of bulk CeO_2 (464 cm^{-1}) [54]. It is speculated that both nanocrystallite size and structural defects in ceria species dispersed affect the position of the F_{2g} mode [55,56]. The signals at $1150\text{-}1060\text{ cm}^{-1}$ and at $880\text{-}860\text{ cm}^{-1}$ appearing solely for non-treated Ce-H- β^T and further for oxidized Ce-H- β and Ce-H- β^T are associated with the O—O stretching vibration mode of surface adsorbed superoxide (O_2^-) [57] and peroxide O_2^{2-} [58] anions, respectively. These superoxide O_2^- and peroxide O_2^{2-} moieties are formed by the interaction of the surface adsorbed oxygen with the electron trapped in the oxygen vacancy and they are indicative for the presence of highly active redox couple $\text{Ce}^{4+}/\text{Ce}^{3+}$. The highest amount of reactive oxygen species appear on the samples Ce-H- β and Ce-H- β^T and the lowest on Ce- SiO_2 and Ce- Al_2O_3 signifying that the presence of Brønsted acid sites enables the formation of superoxide (O_2^-) and peroxide O_2^{2-} anions. The enhancement of catalytic productivity due to the presence of O_2^- and O_2^{2-} sites were reported for hydrotalcite-like compounds hosting metal catalysts, such as Mg(Fe/Al), Ni(Fe/Al) and Co(Fe/Al) [22]. Unquestionably, the role of oxidative properties of O_2^- and O_2^{2-} anions was evidenced by using undoped mayenite as catalyst for the total oxidation of gaseous TCE [59].

3.2.4. EPR spectroscopy

The electron paramagnetic resonance (EPR) spectroscopy provides direct proof for the highly dispersed state of ceria in all the materials studied. EPR is a method to detect radicals adsorbed on the catalysts surface as well as transition metal species dispersed on various supports [60,61]. The combination of an elevated oxygen transport capacity coupled with the ability to shift easily between reduced and oxidized states in redox couple $\text{Ce}^{4+}/\text{Ce}^{3+}$ as well as the ability of the O uptake/release and the influence of the preparation procedure on the above properties was evidenced by EPR spectroscopy (Fig.SI.3). As mentioned above, O_2^- surface species were identified by Raman spectroscopy. Evidence for the presence of superoxide radicals was also obtained by EPR studies. The EPR signals typical for such radicals were observed for all investigated samples after oxygen adsorption [62]. On the basis of computer simulations, the spectra consist of two, O-EPR and R-EPR, overlapping signals characterized by $g_z = 2.024\text{-}2.027$, $g_x = 2.016\text{-}2.019$, $g_y = 2.011\text{-}2.012$ and $g \cong 2.003$, respectively (Table 3). The order of the g values $g_z > g_x > g_y$ results from the convention adopted in the literature [51]. The calculated g parameters for the O-EPR slightly vary between samples, however, they are very close to those described in literature for superoxide radicals adsorbed on similar materials containing metal species [40,51,62]. The variation of the g parameters is attributed to the different chemical environment of the Ce sites, where oxygen is chemisorbed [51]. The observed g_x

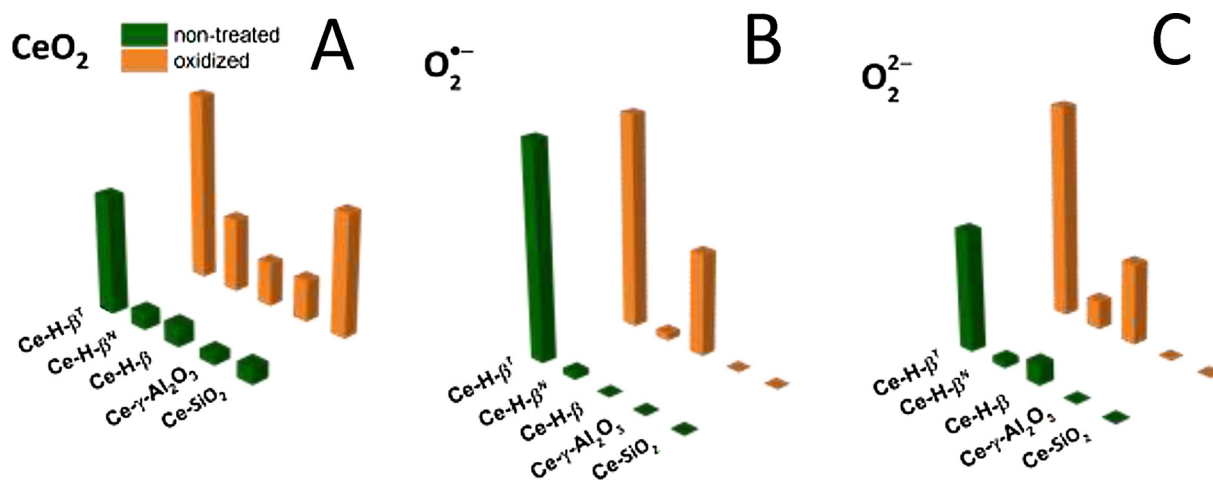


Fig. 4. The intensity of F_{2g} mode of bulk CeO₂ at 440–460 cm⁻¹ (A), superoxide anion (O₂^{·-}) at ~1100 cm⁻¹ (B) and peroxide anion (O₂²⁻) at 880 cm⁻¹ (C) observed for as made and the oxidized form of catalysts.

Table 3

Characteristics^a of the EPR signals obtained upon oxygen adsorption on the outgassed samples.

	superoxide radicals		Ce ³⁺		
	g _z	g _x	g _y	g _⊥	g
Ce-H-β ^T	2.024	2.018	2.011	1.966	1.937
Ce-H-β	2.025	2.016	2.011	1.965	1.937
Ce-H-β ₅₅₀	2.024	2.019	2.011	1.966	1.938
Ce-H-β ₅₅₀ ^N	2.024	2.018	2.011	1.965	1.934
Ce-SiO ₂	2.027	2.016	2.011	1.965	1.934
Ce-Al ₂ O ₃	2.027	2.017	2.012	1.964	1.937
Average:	~2.025	~2.017	~2.011	~1.965	~1.936

^a Obtained by computer simulation of the spectra. (Fig_SI.4).

value is considerably higher than free electron g value (2.0023), indicating the partially covalent character of the superoxide-metal centre bond.

The g_z value of superoxide radicals is the most sensitive to an effective charge of the adsorption centres [62]. In this case, the net charge of cerium ions might be correlated with the size of nanoparticles. In the ideal macroscopic crystal, Ce⁴⁺ ions are balanced by O²⁻ ions charge. However, for very small nanocrystals or ions in exchange position some unneutralized charge will be present. Such sites exhibit slightly different effective charges, also different values of the g_z component. The changes observed in the g_z are in good agreement with particles sizes determined by TEM measurements. The small g_z values (2.024–2.025) are observed for the samples with particles size 12 nm, whereas for the nanoparticles equal to or bigger than 5 nm g_z increase to 2.027. Further, the presence of Brønsted acid can modify an effective charge of the nearest neighbourhood of Ce sites thus g_z value of superoxide radicals. Recent research has shown that the catalytic oxidation of DCE over CeO₂/HZSM-5 catalysts was promoted obviously due to the synergy between acid sites and oxygen mobility [63,64]. The signal denoted R-EPR is assigned to the matrix defect created upon samples activation [61]. In addition to described above overlapping signals, separated one, denoted Ce-EPR, characterized by g_⊥ ≈ 1.965 and g_{||} ≈ 1.936 can be seen in EPR spectra. This signal is typically assigned to Ce³⁺ ions formed by ceria reduction [65,66]. In such the case an oxygen atom is removed from the lattice position, remaining two electrons reduce Ce⁴⁺ into Ce³⁺ and the formation of the close pair Ce³⁺–V_O^{·-}–Ce³⁺ occurs. However, due to the strong spin-spin interaction, the ground state of such pair would be a singlet (S = 0), and at temperatures, at which the population of the triplet states would be large, the observation of the signal by X-Band CW-EPR technique would be impossible because of

the high rate of spin-lattice relaxation [67]. The V_O sites exist as structural defects in stoichiometric CeO₂ [68] or can be formed by the loss of surface oxygen lattice in CeO₂ at high temperatures above 530 °C [69]. Removal of oxygen from ceria at high temperatures, in fact, leads to the formation of a continuum of O-deficient (Ce³⁺–V_O^{·-}–Ce³⁺) nonstoichiometric compositions of the type CeO_{2-x}. This is in an agreement with our observation that the Ce-EPR signal is not visible after activation under vacuum at 450 °C (Fig_SI. 3), however, appearing after oxygen adsorption together with the signal of superoxide radicals. This phenomenon can be rationalized by the assumption, that upon oxygen adsorption the O₂ molecule preferentially adsorbs on Ce³⁺ centers. Then an electron from Ce³⁺ ion is transferred to the π_g* orbital of O₂ molecule [70] and O₂^{·-} radical is formed (Fig_SI.4). Oxidation of Ce³⁺ to Ce⁴⁺ lead to the transformation of Ce³⁺–V_O^{·-}–Ce³⁺ pair to Ce³⁺–V_O^{·-}–Ce⁴⁺ one, which was detected by EPR (Fig_SI. 4). The formation of superoxide is symptomatic for the existence of low-coordinated Ce³⁺ ions on the surface of the ceria nanoparticles [70]. The EPR studies evidence various responses of microporous Ce-H-β and hierarchical zeolites Ce-H-β and Ce-H-β^N for the oxygen treatment. The quantification of both Ce³⁺ sites and radicals was not attainable in our experimental conditions however the role of the support in the cerium-oxide species is clearly evidenced.

3.3. Catalytic activity results

The catalysts were evaluated for the TCE oxidation by monitoring the conversion as a function of the temperature. The results for the H- and Ce-zeolites BEA are presented in Fig. 5A and they are compared with those obtained with a Ce supported silica.

The catalytic activity of the SiO₂, that does not present acidity, started at around 400–450 °C and rose up to 45% of TCE conversion at 550 °C. Deposition of cerium slightly modifies the catalytic activity and the conversion of TCE reached 67% at 550 °C. The application of H-β zeolite results in a much better activity probably because of the presence of acidic centres in the zeolite that strongly affects the adsorption of TCE and the subsequent reaction, starting the TCE oxidation at a lower temperature (350 °C) and obtaining an 82% of the TCE conversion at 550 °C. The Ce-deposition in H-zeolites significantly shifts the catalytic activity to lower temperature: the TCE oxidation starts below 250 °C reaching 100% conversion at 450 °C for the Ce-zeolites studied (Fig. 5A). Nevertheless, a positive influence of the generated mesoporosity is observed in the low-temperature range, i.e. 250–325 °C. The shortened diffusion path due to secondary mesoporosity fabrication assures effective contact of DCE or HCl molecules with CeO₂ with high activity for Deacon reaction. On the other hand, mild steamed zeolites

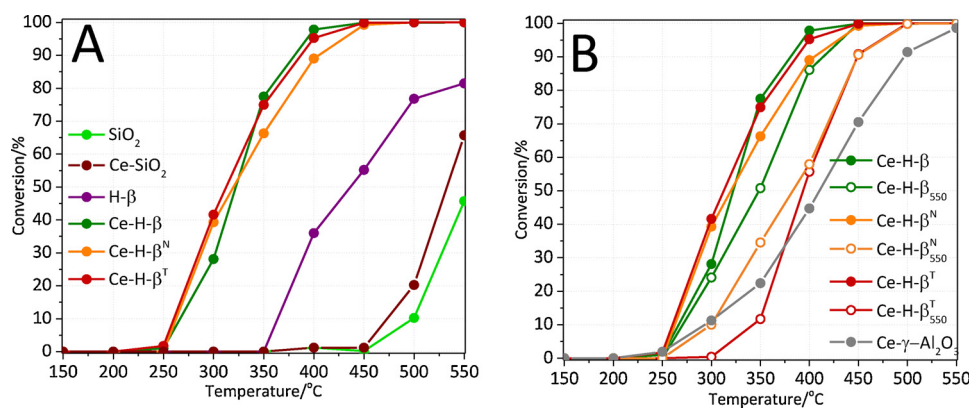


Fig. 5. TCE conversion with all the materials studied.

(at 550 °C) (Fig. 5B) present a drop of the conversion and this is more pronounced for the mesoporous zeolites. This can be associated with the transformation of Brønsted to Lewis acid sites observed in all the Ce-zeolites after the steaming treatment (as discussed in Section 3.2.2). Nevertheless, the Lewis acid moieties also take part in the reaction, as is evidenced by the results obtained with the $\text{Ce-}\gamma\text{-Al}_2\text{O}_3$, a sample that only presents Lewis acidity (Table 2). However it is clear that the impact of Brønsted acidity is more significant. In this way, in mildly steamed mesoporous zeolites the silanol groups perturbed by neighbouring electron acceptor aluminium species might have an impact on protonic acidity and for this reason, a better activity is obtained with the Ce-zeolites that with the Ce-alumina or Ce-silica.

The Brønsted acidity was reported to play a key role in TCE oxidation since the process is initiated by the chemisorption on Brønsted sites and protonation of the chlorinated molecule [71,72]. Together with this, the reactions of oxygen molecules adsorbed at V_o sites detected by EPR are also essential to recover the catalytic activity of ceria by transforming adsorbed TCE-originated species into oxygenated species and/or by filling in the oxygen vacant sites. Several contradicting factors, however, seem to contribute to the overall role of vacant oxygen sites in promoting versus suppressing the catalytic effect toward decomposition of Cl-VOGs. It has been demonstrated by the DFT approach [73] that the presence of Ce(III) gives the rise to the electron affinity for Ce atoms adjacent to the surface oxygen vacant site V_o . This, in turn, is reflected by a lower activation barrier and higher exothermicity for the C-Cl bond fission. Then a clear impact of the acid/base characteristics of the support on the redox $\text{Ce}^{4+}/\text{Ce}^{3+}$ pair potential is expected.

Among the zeolites studied the non-steamed Ce-zeolites combines distinctive properties regarding highly developed mesopore surface area (Table 1), high dispersion of the cerium species (Fig. 2) with high number of Brønsted sites preserved (Table 2), higher amount of active oxygen species measured by EPR and finally overall high concentration of acid sites (Table 2) offering the best catalytic activity. Since the protonic acidity is involved in the chemisorption and the further transformations of TCE molecules the strength of the protonic sites seems to be the decisive factor influencing the activity of the catalyst. The results obtained with these catalysts compared with other materials show a better activity than Cu or Co-zeolites [11], mayenite [74,75] or mixed oxides [14].

The different products distribution in the conversion of TCE is shown in Fig. 6 over the most active zeolites $\text{Ce-H-}\beta^T$ (A, B) and $\text{Ce-H-}\beta$ (C, D) calcined at 450 °C (A,C) and 550 °C (B,D). In all cases, the main oxidation products obtained in the TCE oxidation were CO, CO_2 , and HCl. The redox properties of the catalysts favoured the complete oxidation of the carbon species at temperatures as high as 450–500 °C. Low amounts of Cl_2 were detected only at temperatures above 450 °C, this can be related with the presence of surface OH groups in the zeolite that prevented the formation of Cl_2 , in line with Karmakar and Greene [71]

reports. The hydrochloric acid was the main chlorinated product obtained from the beginning of the reaction. The formation of HCl requires the source of H-atoms that can be provided by the available H-rich moieties, by the trichloroethylene, by the zeolitic protonic sites or by water impurities in the gas stream [18]. Then, the formation of HCl in dry experimental conditions suggests that the zeolite hydroxyls in the structure largely promoted HCl formation. Additionally, the formation of AlCl_3 could be considered as another reason for the declined selectivity to Cl_2 . The realumination process, inherent to desilication, is responsible for the enrichment of the grain's surface in aluminium, known as an Al-rich shell. These reinserted into the framework Al atoms undergo leaching in the presence of chlorine molecules. Tetrachloroethylene (C_2Cl_4) was detected in the temperature region of 300–500 °C.

The carbon and chlorine selectivities are shown in Table 4. The Ce-zeolites calcined at 450 °C present higher selectivity to CO than the catalysts steamed at 550 °C. Obviously, this may be due to the fact that 50% conversion is obtained at higher temperatures for more selective CO_2 catalysts (Figs. 6 and 7), nevertheless, higher dispersion of cerium species in the zeolites with higher number of Brønsted sites (Table 2) can also favour CO formation. The presence of bulk cerium oxide results in higher ability to oxidize CO to CO_2 by its higher oxygen storage capacity in the bulk of CeO_2 -particles comparing with small clusters. It is line with the highest selectivity to CO_2 observed for $\text{Ce-}\gamma\text{-Al}_2\text{O}_3$ characterized by the lowest dispersion (Fig. 2) of cerium oxyhydroxide microphase (Fig. 1). The amount of formed CO_2 can be discussed in term of the strength of the Si(OH)Al acid sites. Taking into account the particular value of CO_2 selectivity (ca. 25%), it can be observed that the similar amounts of CO_2 are achieved in the lowest temperature (300 °C) by the hierarchical zeolites $\text{Ce-H-}\beta^T$ and $\text{Ce-H-}\beta^N$ with sites of the medium strength. More pronounced reduction of the strength of protonic moieties in mildly steamed $\text{Ce-H-}\beta_{550}^T$ and $\text{Ce-H-}\beta_{550}^N$ offers nearly the same selectivity to CO_2 , but this is obtained at a higher temperature (around 400 °C). This can suggest that the hydroxyl groups on the catalyst surface, mainly Si(OH)Al , are also responsible for bonding of intermediate product i.e. CO molecules and its further oxidation to CO_2 , besides their crucial role in TCE molecule chemisorption. Indeed, the Brønsted acid sites have been reported to determine the nature of the carbon-based intermediates formed upon the CO oxidation over copper oxide-cerium oxide catalysts [76]. Hydroxyl groups are believed to favour the formation of surface bicarbonates, then their facile decomposition to CO_2 . It could be also possible that CO_2 produced at cerium-oxide active sites is transferred to hydroxyls in a further step, leaving the cerium-oxide sites available again. In fact, the dependence of selectivity to CO_2 on the number and strength of Brønsted acid sites (Table 2, Fig. 7) seems to provide the evidence to support the former hypothesis.

On the chlorinated products, the samples calcined at 450 °C show lower selectivity to tetrachloroethylene and Cl_2 and higher to

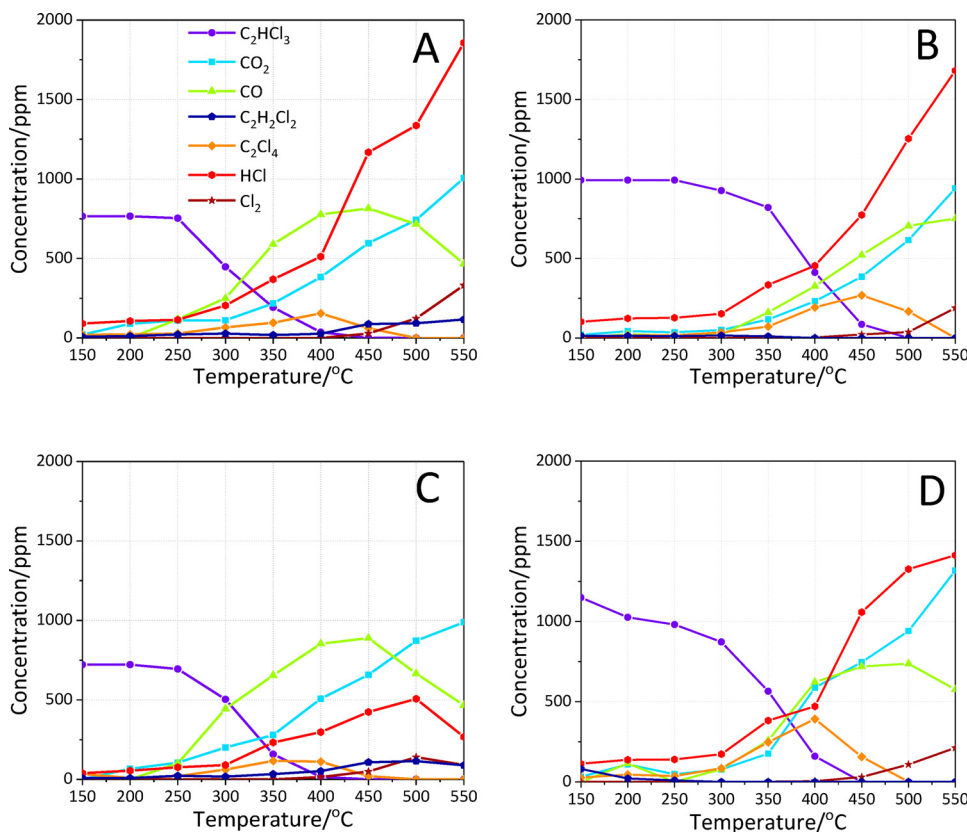


Fig. 6. Product distribution in the TCE oxidation reaction over the most active zeolites Ce-H- β^T (A, B) and Ce-H- β (C, D) calcined at 450 °C (A, C) and at 550 °C (B, D).

Table 4
Selectivities for TCE oxidation products at a temperature close to 50% conversion.

Samples	Selectivity to carbon mol%				Selectivity to chlorine mol%			
	CO ₂	CO	C ₂ H ₂ Cl ₂	C ₂ Cl ₄	HCl	Cl ₂	C ₂ H ₂ Cl ₂	C ₂ Cl ₄
	CO ₂	CO	C ₂ H ₂ Cl ₂	C ₂ Cl ₄	HCl	Cl ₂	C ₂ H ₂ Cl ₂	C ₂ Cl ₄
Ce-H- β	23.1	54.2	2.8	19.8	29.8	0.0	8.7	61.5
Ce-H- β_{550}	19.0	27.7	0.0	53.3	27.8	0.2	0.0	72.0
Ce-H- β^N	22.0	46.3	4.3	27.4	37.7	0.0	8.4	53.9
Ce-H- β_{550}^N	24.2	34.8	0.0	41.0	34.1	0.3	0.0	65.6
Ce-H- β^T	21.3	47.9	5.2	25.6	38.8	0.0	10.4	50.8
Ce-H- β_{550}^T	24.5	34.6	0.0	40.9	36.9	0.5	0.0	62.6
Ce-SiO ₂	29.6	29.5	40.9	0.0	42.2	0.1	57.6	0.0
Ce- γ -Al ₂ O ₃	48.1	35.9	16.0	0.0	51.3	3.0	45.7	0.0

dichloroethylene and HCl when comparing at the constant conversion of 50% (Table 4 and Fig. 8).

The formation of tetrachloroethylene comes from the chlorination of TCE by Cl₂ or by transchlorination reaction between two TCE molecules and not from the reaction with HCl that is not a very effective chlorination agent. At 50% conversion, only small amount of Cl₂ is detected in the products due to the fast conversion of Cl₂ to HCl or tetrachloroethylene. In absence of water, HCl is formed by hydrogen abstraction by chlorine from the hydroxyls of the surface of zeolite according to the reverse Deacon reaction mechanism (Cl₂ + H₂O \leftrightarrow 2HCl + 1/2O₂). Therefore, the presence of high density of hydroxyls causes the conversion of Cl₂ to HCl, thus decreasing its conversion to tetrachloroethylene. In fact, when comparing the selectivity to chlorinated products of the Ce-H- β and the hierarchical samples Ce-H- β^N and Ce-H- β^T these latter show higher selectivity to HCl and lower to tetrachloroethylene whatever the calcination temperature is. In addition, it becomes clear that chlorination reaction requires the presence of

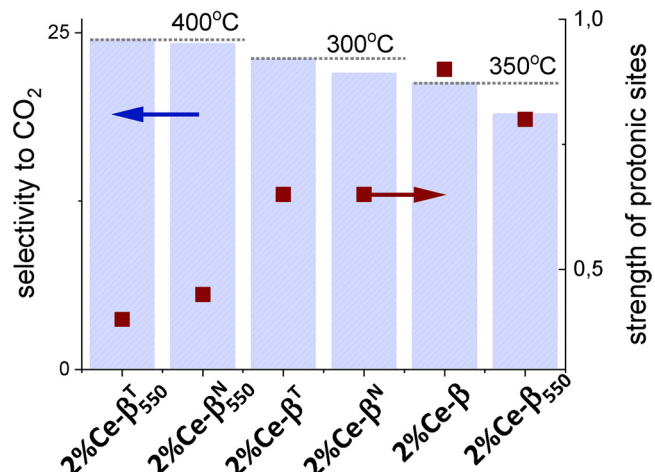


Fig. 7. Selectivity to CO₂ with respect to temperature where reached value of ca. 25% in function of the strength of Brønsted acid sites (from IR thermodesorption studies).

Brønsted acid sites since tetrachloroethylene (C₂Cl₄) is absent in the products of Ce-SiO₂ and Ce-Al₂O₃ with no Brønsted acidity.

The presence of a small amount dichloroethylene in the products of samples of Ce-Beta zeolites calcined at 450 °C should be attributed to the transchlorination reaction between two TCE molecules (2 C₂HCl₃ \leftrightarrow C₂H₂Cl₂ + C₂Cl₄) favoured by the higher Brønsted acid density of these samples comparing with those calcined at 550 °C (Table 2). Again, for this bimolecular reaction similarly as for other disproportionation reactions in zeolites, the presence of a higher density of Brønsted acid sites is required [61,62]. Nevertheless the formation of C₂HCl₂ by dechlorination of TCE on the surface of cerium oxide can not be completely excluded. In the case of Ce-SiO₂ and Ce-Al₂O₃, the high yield of

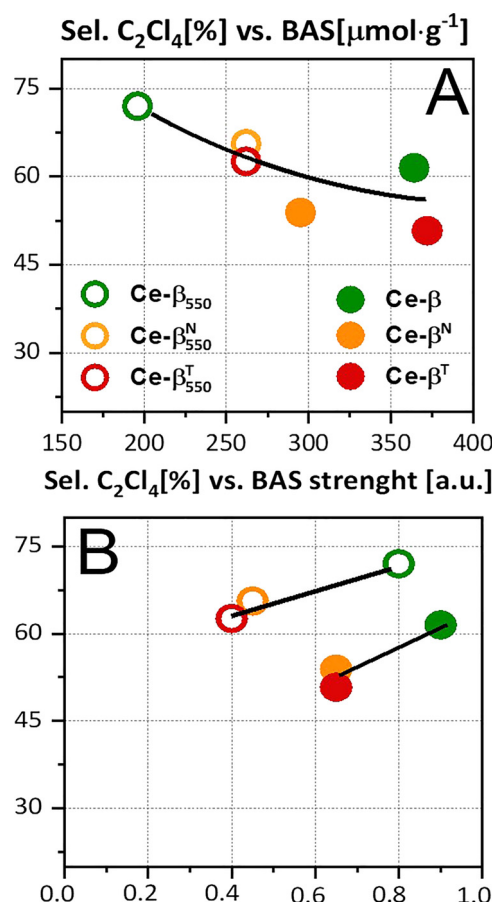


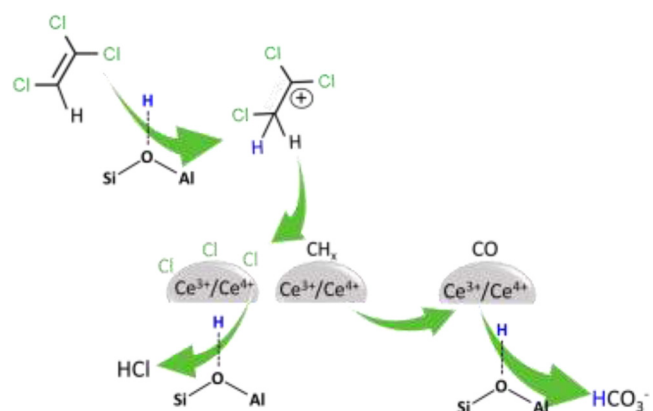
Fig. 8. Selectivity of C_2Cl_4 as the function of Brønsted acid sites concentration (BAS) (A) and their strength (B).

DCE should be due to the dechlorination reaction taking place at a higher temperature than for the Ce-zeolite samples.

The separation of the influence of total BAS acidity and the different acid strength in the selectivity to C_2Cl_4 is shown in Fig. 8 out of data from Table 4. An inverse correlation between the selectivity to C_2Cl_4 and the total BAS acidity can be seen (Fig. 8A). In addition, when comparing at constant BAS strength (Fig. 8B) it is clearly seen that an increase in C_2Cl_4 is obtained for the samples with lower BAS acidity, which are those mildly steamed at a higher temperature of 550°C . It means that the acid strength does not have an important influence on the selectivity of C_2Cl_4 and that it is mainly determined by the number of OH groups with Brønsted acidic character, which act as hydrogen donors for the inverse Deacon reaction increasing the yield of HCl and therefore inhibiting the chlorination reaction of TCE to C_2Cl_4 .

Additional information is found when comparing the selectivities of Ce doped amorphous silica and alumina. The $\text{Ce}-\gamma\text{-Al}_2\text{O}_3$ presents higher selectivity to $\text{CO} + \text{CO}_2$, while Ce-SiO_2 shows lower $\text{CO} + \text{CO}_2$ values and higher selectivity to dichloroethylene whereas no one yields to tetrachloroethylene. These data indicate that the formation of tetrachloroethylene needs the presence of Brønsted acid sites, as manifested by the higher selectivity found for the samples $\text{Ce-H-}\beta$. The higher $\text{CO} + \text{CO}_2$ selectivity of $\text{Ce}-\gamma\text{-Al}_2\text{O}_3$ should be related to the presence of only Lewis acid sites.

An adequate combination of ceria redox and the support's acidic characteristic is beneficial to the high activity catalyst for this reaction. The highly acidic $\text{Si(OH)}\text{Al}$ hydroxyls are the first choice sites for the adsorption of the chlorinated molecule which is the first reaction step [77,78]. In the second step, the $\text{Ce}^{3+}/\text{Ce}^{4+}$ acts as active centres for C-Cl bonds splitting [79]. Consequently, the dissociative CH_x species are oxidized by the active oxygen species to produce H_2O and CO_2 .



Scheme 1. The Brønsted acid site-mediated TCE oxidation route.

Meantime, bicarbonate-mediated oxidation of the carbon-based intermediates formed over cerium species is started over the strongly acidic Brønsted acid sites. Further, a fabricated mesoporosity benefits to a short contact of chlorinated molecules with CeO_2 with high activity for Deacon reaction. The mechanism of process is presented in Scheme 1.

4. Conclusions

Higher dispersion of cerium with a higher amount of reactive oxygen species have been obtained in zeolite Beta by impregnation of hierarchical samples obtained by caustic and thermal treatment with NaOH and TBAOH. These samples have shown high activity at low temperature for the oxidation of TCE. The effect of total BAS acidity, silanol groups, and acid strength has been studied. The number of high strength Brønsted acid centres located in Ce-loaded zeolites framework was found to be an important factor influencing the activity and selectivity of catalysts as well as combination of mesoporosity and Brønsted acidity maximizes the activity of Ce-Beta samples for the oxidation of TCE.

Declaration of Competing Interest

The authors declare that they have no known competing financial interests or personal relationships that could have appeared to influence the work reported in this paper.

Acknowledgement

The work was financed by the Grant No. <GN1> 2015/18/E/ST4/00191 from the National Science Centre, Poland. J.M.T. and A.E.P. thank Spanish Government through "Severo Ochoa" <GN2> SEV-2016-0683, <GN2> RTI2018-099668-B-C21, <GN2> RTI2018-101784-B-I00 and the Foundation Ramón Areces through a research contract of the "Life and Materials Science" program.

Appendix A. Supplementary data

Supplementary material related to this article can be found, in the online version, at doi:<https://doi.org/10.1016/j.apcatb.2019.118022>.

References

- [1] A.R. Gavaskar, B.C. Kim, S.H. Rosansky, S.K. Ong, E.G. Marchand, Crossflow air stripping and catalytic oxidation of chlorinated hydrocarbons from groundwater, Environ. Prog. 14 (2018) 33–40, <https://doi.org/10.1002/ep.670140119>.
- [2] A. Yasuhara, M. Morita, Formation of chlorinated compounds in pyrolysis of trichloroethylene, Chemosphere 21 (1990) 479–486, [https://doi.org/10.1016/0045-6535\(90\)90018-O](https://doi.org/10.1016/0045-6535(90)90018-O).
- [3] M. Kosusko, M.E. Mullins, K. Ramanathan, T.N. Rogers, Catalytic oxidation of

- groundwater stripping emissions, Environ. Prog. 7 (1988) 136–142, <https://doi.org/10.1002/ep.3300070216>.
- [4] R.K. Shah, B. Thonon, D.M. Benforado, Opportunities for heat exchanger applications in environmental systems, Appl. Therm. Eng. 20 (2000) 631–650, [https://doi.org/10.1016/S1359-4311\(99\)00045-9](https://doi.org/10.1016/S1359-4311(99)00045-9).
- [5] S. Santos, K. Jones, R. Abdul, J. Boswell, J. Paca, Treatment of wet process hardboard plant VOC emissions by a pilot scale biological system, Biochem. Eng. J. 37 (2007) 261–270, <https://doi.org/10.1016/j.bej.2007.05.005>.
- [6] R.E. Hester, R.M. Harrison, Volatile Organic Compounds in the Atmosphere, Royal Society of Chemistry, 1995, <https://doi.org/10.1002/9780470988657>.
- [7] W.B. Li, W.B. Chu, M. Zhuang, J. Huo, Catalytic oxidation of toluene on Mn-containing mixed oxides prepared in reverse microemulsions, Catal. Today 93 (2004) 205–209, [https://doi.org/10.1016/0926-860X\(92\)85009-Z](https://doi.org/10.1016/0926-860X(92)85009-Z).
- [8] J.J. Spivey, Complete catalytic oxidation of volatile organics, Ind. Eng. Chem. Res. 26 (1987) 2165–2180, <https://doi.org/10.1021/ie00071a001>.
- [9] S.K. Agarwal, J.J. Spivey, J.B. Butt, Catalyst deactivation during deep oxidation of chlorohydrocarbons, Appl. Catal. A Gen. 82 (1992) 259–275, [https://doi.org/10.1016/0926-860X\(92\)85009-Z](https://doi.org/10.1016/0926-860X(92)85009-Z).
- [10] S.C. Petrosius, R.S. Drago, V. Young, G.C. Grunewald, Low-temperature decomposition of some halogenated hydrocarbons using metal oxide/porous carbon catalysts, J. Am. Chem. Soc. 115 (1993) 6131–6137, <https://doi.org/10.1021/ja00067a031>.
- [11] N. Blanch-Raga, A.E. Palomares, J. Martínez-Triguero, G. Fetter, P. Bosch, Cu mixed oxides based on hydrotalcite-like compounds for the oxidation of trichloroethylene, Ind. Eng. Chem. Res. 52 (2013) 15772–15779, <https://doi.org/10.1021/ie4024935>.
- [12] N. Blanch-Raga, A.E. Palomares, J. Martínez-Triguero, M. Puche, G. Fetter, P. Bosch, The oxidation of trichloroethylene over different mixed oxides derived from hydrotalcites, Appl. Catal. B Environ. 160–161 (2014) 129–134, <https://doi.org/10.1016/j.apcatb.2014.05.014>.
- [13] S.H. Taylor, C.S. Heneghan, G.J. Hutchings, I.D. Hudson, The activity and mechanism of uranium oxide catalysts for the oxidative destruction of volatile organic compounds, Catal. Today 59 (2000) 249–259, [https://doi.org/10.1016/S0920-5861\(00\)00291-1](https://doi.org/10.1016/S0920-5861(00)00291-1).
- [14] J. Carpenterier, J.-F. Lamontier, S. Siffert, H. Laversin, A. Aboukaïs, Preparation and characterization of Co–Fe–Cu mixed oxides via hydrotalcite-like precursors for toluene catalytic oxidation, Stud. Surf. Sci. Catal. Elsevier, 2007, pp. 1197–1204, [https://doi.org/10.1016/s0167-2991\(02\)80280-4](https://doi.org/10.1016/s0167-2991(02)80280-4).
- [15] V.R. Choudhary, G.M. Deshmukh, S.G. Pataskar, Low temperature complete combustion of dilute toluene and methyl ethyl ketone over transition metal-doped ZrO₂ (cubic) catalysts, Catal. Commun. 5 (2004) 115–119, <https://doi.org/10.1016/j.catcom.2003.12.003>.
- [16] W.B. Li, J.X. Wang, H. Gong, Catalytic combustion of VOCs on non-noble metal catalysts, Catal. Today 148 (2010) 81–87, <https://doi.org/10.1016/j.cattod.2009.03.007>.
- [17] G.A. Atwood, H.L. Greene, P. Chintawar, R. Rachapudi, B. Ramachandran, C.A. Vogel, Trichloroethylene sorption and oxidation using a dual function sorbent/catalyst in a falling furnace reactor, Appl. Catal. B Environ. 18 (1998) 51–61, [https://doi.org/10.1016/S0926-3373\(98\)00023-X](https://doi.org/10.1016/S0926-3373(98)00023-X).
- [18] J.R. González-Velasco, R. López-Fonseca, A. Aranzabal, J.I. Gutiérrez-Ortiz, P. Steltenpohl, Evaluation of H-type zeolites in the destructive oxidation of chlorinated volatile organic compounds, Appl. Catal. B Environ. 24 (2000) 233–242, [https://doi.org/10.1016/S0926-3373\(99\)00105-8](https://doi.org/10.1016/S0926-3373(99)00105-8).
- [19] L. Intriago, E. Díaz, S. Ordóñez, A. Vega, Combustion of trichloroethylene and dichloromethane over protonic zeolites: influence of adsorption properties on the catalytic performance, Microporous Mesoporous Mater. 91 (2006) 161–169, <https://doi.org/10.1016/j.micromeso.2005.11.043>.
- [20] R. López-Fonseca, B. De Rivas, J.I. Gutiérrez-Ortiz, A. Aranzabal, J.R. González-Velasco, Enhanced activity of zeolites by chemical dealumination for chlorinated VOC abatement, Appl. Catal. B Environ. 41 (2003) 31–42, [https://doi.org/10.1016/S0926-3373\(02\)00199-6](https://doi.org/10.1016/S0926-3373(02)00199-6).
- [21] A. Aranzabal, B. Pereda-Ayo, M.P. González-Marcos, J.A. González-Marcos, R. López-Fonseca, J.R. González-Velasco, State of the art in catalytic oxidation of chlorinated volatile organic compounds, Chem. Pap. 68 (2014) 1169–1186, <https://doi.org/10.2478/s11696-013-0505-7>.
- [22] N. Blanch-Raga, A.E. Palomares, J. Martínez-Triguero, S. Valencia, Cu and Co modified beta zeolite catalysts for the trichloroethylene oxidation, Appl. Catal. B Environ. 187 (2016) 90–97, <https://doi.org/10.1016/j.apcatb.2016.01.029>.
- [23] A.P. Antunes, M.F. Ribeiro, J.M. Silva, F.R. Ribeiro, P. Magnoux, M. Guisnet, Catalytic oxidation of toluene over CuNaHY zeolites, Appl. Catal. B Environ. 33 (2001) 149–164, [https://doi.org/10.1016/s0926-3373\(01\)00174-6](https://doi.org/10.1016/s0926-3373(01)00174-6).
- [24] B. de Rivas, C. Sampedro, R. López-Fonseca, M.Á. Gutiérrez-Ortiz, J.I. Gutiérrez-Ortiz, Low-temperature combustion of chlorinated hydrocarbons over CeO₂/H-ZSM5 catalysts, Appl. Catal. A Gen. 417–418 (2012) 93–101, <https://doi.org/10.1016/J.APCATA.2011.12.028>.
- [25] S. Lutfalla, V. Shapovalov, A.T. Bell, Calibration of the DFT/GGA+U method for determination of reduction energies for transition and rare earth metal oxides of Ti, V, Mo, and Ce, J. Chem. Theory Comput. 7 (2011) 2218–2223, <https://doi.org/10.1021/ct200202g>.
- [26] T. Zhu, L. Kundakovic, A. Dreher, M. Flytzani-Stephanopoulos, Redox chemistry over CeO₂-based catalysts: SO₂ reduction by CO or CH₄, Catal. Today 50 (1999) 381–397, [https://doi.org/10.1016/S0920-5861\(98\)00517-3](https://doi.org/10.1016/S0920-5861(98)00517-3).
- [27] J. Tan, W. Zhang, Y.-H. Lv, A.-L. Xia, Facile preparation of Mn-doped CeO₂ Submicrorods by composite-hydroxide-salt-mediated approach and their magnetic property, Mater. Res. 16 (2013) 689–694, <https://doi.org/10.1590/s1516-14392013005000040>.
- [28] Q. Shen, G. Lu, C. Du, Y. Guo, Y. Wang, Y. Guo, X. Gong, Role and reduction of NO_x in the catalytic combustion of soot over iron-ceria mixed oxide catalyst, Chem. Eng. J. 218 (2013) 164–172, <https://doi.org/10.1016/j.cej.2012.12.010>.
- [29] P.H. Taylor, D.A. Tirey, W.A. Rubey, B. Dellinger, Detailed Modeling of the Pyrolysis of Trichloroethene: Formation of Chlorinated Aromatic Species, Combust. Sci. Technol. 101 (1994) 75–102, <https://doi.org/10.1080/00102209408951867>.
- [30] M. Altarawneh, B.Z. Dlugogorski, Formation of dibenzofuran, dibenzo-p-dioxin and their hydroxylated derivatives from catechol, Phys. Chem. Chem. Phys. 17 (2015) 1822–1830, <https://doi.org/10.1039/c4cp04168b>.
- [31] H.A.A. Miran, M. Altarawneh, H. Widjaja, Z.N.N. Jaf, M.M. Rahman, J.-P. Veder, B.Z.Z. Dlugogorski, Z.-T. Jiang, M. Mahbubur Rahman, J.-P. Veder, B.Z.Z. Dlugogorski, Z.-T. Jiang, Thermo-mechanical properties of cubic lanthanide oxides, Thin Solid Films 653 (2018) 37–48, <https://doi.org/10.1016/J.TSF.2018.01.063>.
- [32] M. Tajima, M. Niwa, Y. Fujii, Y. Koinuma, R. Aizawa, S. Kushiyama, S. Kobayashi, K. Mizuno, H. Ohfuchi, Decomposition of chlorofluorocarbons in the presence of water over zeolite catalyst, Appl. Catal. B Environ. 9 (1996) 167–177, [https://doi.org/10.1016/0926-3373\(96\)90079-X](https://doi.org/10.1016/0926-3373(96)90079-X).
- [33] S. Karmakar, H.L. Greene, Characterization of H-Y and Cr-Y zeolite catalysts during the oxidative destruction of CFC11 and CFC12, J. Catal. 148 (1994) 524–533, <https://doi.org/10.1006/jcat.1994.1238>.
- [34] M. Briend-Faure, O. Cornu, D. Delafosse, R. Monque, M.J. Peltre, Chemical and thermal stability of dealuminated faujasite-type zeolites in gaseous and aqueous phases, Appl. Catal. 38 (1988) 71–87, [https://doi.org/10.1016/S0166-9834\(00\)80987-2](https://doi.org/10.1016/S0166-9834(00)80987-2).
- [35] M. Müller, G. Harvey, R. Prins, Comparison of the dealumination of zeolites beta, mordenite, ZSM-5 and ferrierite by thermal treatment, leaching with oxalic acid and treatment with SiCl₄ by 1H, 29Si and 27Al MAS NMR, Microporous Mesoporous Mater. 34 (2000) 135–147, [https://doi.org/10.1016/S1387-1811\(99\)00167-5](https://doi.org/10.1016/S1387-1811(99)00167-5).
- [36] J.C. Groen, J.A. Moulijn, J. Pérez-Ramírez, Desilication: on the controlled generation of mesoporosity in MFI zeolites, J. Mater. Chem. 16 (2006) 2121–2131, <https://doi.org/10.1039/b517510k>.
- [37] J. Datka, J.M. Triguero, F. Rey, K. Sadowska, K. Góra-marek, M. Drozdek, P. Kus, Microporous and Mesoporous Materials Desilication of highly siliceous zeolite ZSM-5 with NaOH and NaOH/tetrabutylamine hydroxide, Direct 168 (2013) 195–205, <https://doi.org/10.1016/j.micromeso.2012.09.033>.
- [38] K. Sadowska, K. Góra-Marek, J. Datka, Hierarchic zeolites studied by IR spectroscopy: acid properties of zeolite ZSM-5 desilicated with NaOH and NaOH/tetrabutylamine hydroxide, Vib. Spectrosc. 63 (2012) 418–425, <https://doi.org/10.1016/j.vibspec.2012.09.007>.
- [39] K. Góra-Marek, M. Derewiński, P. Sarv, J. Datka, IR and NMR studies of mesoporous alumina and related aluminosilicates, Catal. Today 101 (2005) 131–138, <https://doi.org/10.1016/j.cattod.2005.01.010>.
- [40] T. Spałek, P. Pietrzak, Z. Sojka, Application of genetic algorithm for extraction of the parameters from powder EPR spectra, Acta Phys. Pol. A 108 (2005) 95–102, <https://doi.org/10.12693/APhysPolA.108.95>.
- [41] L. Ren, L. Zhu, C. Yang, Y. Chen, Q. Sun, H. Zhang, C. Li, F. Nawaz, X. Meng, F.S. Xiao, Designed copper-amine complex as an efficient template for one-pot synthesis of Cu-SZ-13 zeolite with excellent activity for selective catalytic reduction of NO_x by NH₃, Chem. Commun. 47 (2011) 9789–9791, <https://doi.org/10.1039/c1cc12469b>.
- [42] J.-H. Hwang, T.O. Mason, Defect chemistry and transport properties of nanocrystalline cerium oxide, Zeitschrift Für Phys. Chemie 207 (2011) 21–38, https://doi.org/10.1524/zpch.1998.207.part_1.2.021.
- [43] F. Giordano, A. Trovarelli, C. De Leitenburg, M. Giona, A model for the temperature-programmed reduction of low and high surface area ceria, J. Catal. 193 (2000) 273–282, <https://doi.org/10.1006/jcat.2000.2900>.
- [44] J.M. Rynkowski, T. Paryjczak, A. Lewicki, I. Szynkowska, T. Maniecki, W. Jozwiak, Characterization of Ru/CeO₂-Al₂O₃ catalyst and their performance in CO₂ methanation, React. Kinet. Catal. Lett. 71 (2000) 55–64, <https://doi.org/10.1023/A:1010326031095>.
- [45] L. Katta, P. Sudarsanam, G. Thrimurthulu, B.M. Reddy, Doped nanosized ceria solid solutions for low temperature soot oxidation: zirconium versus lanthanum promoters, Appl. Catal. B Environ. 101 (2010) 101–108, <https://doi.org/10.1016/j.apcatb.2010.09.012>.
- [46] Y. Zhang, M. Flytzani-Stephanopoulos, Hydrothermal stability of cerium modified Cu-ZSM-5 catalyst for nitric oxide decomposition, J. Catal. 164 (1996) 131–145, <https://doi.org/10.1006/jcat.1996.0369>.
- [47] K. Góra-Marek, J. Datka, IR studies of OH groups in mesoporous aluminosilicates, Appl. Catal. A Gen. 302 (2006) 104–109, <https://doi.org/10.1016/j.apcata.2005.12.027>.
- [48] A. Badri, C. Binet, J.-C. Lavallee, An FTIR study of surface ceria hydroxy groups during a redox process with H₂, J. Chem. Soc. Faraday Trans. 92 (2004) 4669, <https://doi.org/10.1039/f9969204669>.
- [49] C.R. Moreira, M.M. Pereira, X. Alcobé, N. Homs, J. Llorca, J.L.G. Fierro, P. Ramírez de la Piscina, Nature and location of cerium in Ce-loaded Y zeolites as revealed by HRTEM and spectroscopic techniques, Microporous Mesoporous Mater. 100 (2007) 276–286, <https://doi.org/10.1016/j.micromeso.2006.11.019>.
- [50] Z. Wang, Y. Jiang, O. Lafon, J. Trébosc, K. Duk Kim, C. Stampfl, A. Baiker, J.P. Amoureux, J. Huang, Brønsted acid sites based on penta-coordinated aluminum species, Natl. Commun. 7 (2016) 1–5, <https://doi.org/10.1038/ncomms13820>.
- [51] A. Martínez-Arias, M. Fernández-García, L.N. Salamanca, R.X. Valenzuela, J.C. Conesa, J. Soria, Structural and redox properties of Ceria in alumina-supported Ceria catalyst supports, J. Phys. Chem. B 104 (2000) 4038–4046, <https://doi.org/10.1021/jp992796z>.
- [52] J.Z. Shyu, W.H. Weber, H.S. Gandhi, Surface characterization of alumina-supported

- ceria, J. Phys. Chem. 92 (1988) 4964–4970, <https://doi.org/10.1021/j100328a029>.
- [53] A. Trovarelli, M. Boaro, E. Rocchini, C. De Leitenburg, G. Dolcetti, Some recent developments in the characterization of ceria-based catalysts, J. Alloys. Compd. 323–324 (2001) 584–591, [https://doi.org/10.1016/S0925-8388\(01\)01181-1](https://doi.org/10.1016/S0925-8388(01)01181-1).
- [54] J.E. Spanier, R.D. Robinson, F. Zhang, S.W. Chan, I.P. Herman, Size-dependent properties of (formula presented) nanoparticles as studied by Raman scattering, Phys. Rev. B Condens. Matter Mater. Phys. 64 (2001) 2454071–2454078, <https://doi.org/10.1103/PhysRevB.64.245407>.
- [55] I. Kosacki, T. Suzuki, H.U. Anderson, P. Colombari, Raman scattering and lattice defects in nanocrystalline CeO₂ thin films, Solid State Ion. 149 (2002) 99–105, [https://doi.org/10.1016/S0167-2738\(02\)00104-2](https://doi.org/10.1016/S0167-2738(02)00104-2).
- [56] S. Aškrabić, Z. Dohčević-Mitrović, A. Kremenović, N. Lazarević, V. Kahlenberg, Z.V. Popović, Oxygen vacancy-induced microstructural changes of annealed CeO₂ – x nanocrystals, J. Raman Spectrosc. 43 (2012) 76–81.
- [57] T. Taniguchi, T. Watanabe, N. Sugiyama, A.K. Subramani, H. Wagata, N. Matsushita, M. Yoshimura, Identifying defects in ceria-based nanocrystals by UV resonance Raman spectroscopy, J. Phys. Chem. C. 113 (2009) 19789–19793, <https://doi.org/10.1021/jp9049457>.
- [58] V.V. Pushkarev, V.I. Kovalchuk, J.L. D'Itri, Probing defect sites on the CeO₂ surface with dioxygen, J. Phys. Chem. B 108 (2004) 5341–5348, <https://doi.org/10.1021/jp0311254>.
- [59] R. Cuccinello, A. Intiso, S. Castiglione, A. Genga, A. Proto, F. Rossi, Total oxidation of trichloroethylene over mayenite (Ca₁₂Al₁₄O₃₃) catalyst, Appl. Catal. B Environ. 204 (2017) 167–172, <https://doi.org/10.1016/j.apcatb.2016.11.035>.
- [60] K. Dyrek, K. Kruczala, Z. Sojka, S. Schlick, Catalysis on polymer supports: ESR of molybdenum (V) dispersed in poly(acrylic acid) matrices, J. Phys. Chem. 97 (2005) 9196–9200, <https://doi.org/10.1021/j100138a021>.
- [61] K.A. Tarach, A. Śrębowata, E. Kowalewski, K. Gołąbek, A. Kostuch, K. Kruczala, V. Girman, K. Góra-Marek, Nickel loaded zeolites FAU and MFI: characterization and activity in water-phase hydrodehalogenation of TCE, Appl. Catal. A Gen. 568 (2018) 64–75, <https://doi.org/10.1016/j.apcata.2018.09.026>.
- [62] K. Sobańska, A. Krasowska, T. Mazur, K. Podolska-Serafin, P. Pietrzak, Z. Sojka, Diagnostic features of EPR spectra of superoxide intermediates on catalytic surfaces and molecular interpretation of their G and A tensors, Top. Catal. 58 (2015) 796–810, <https://doi.org/10.1007/s11244-015-0420-y>.
- [63] Q. Dai, X. Wang, G. Lu, Low-temperature catalytic combustion of trichloroethylene over transition metal-cerium mixed oxide catalysts, Adv. Mater. 81 (2008) 3–4, <https://doi.org/10.1016/j.apcatb.2007.12.013>.
- [64] B. de Rivas, C. Sampedro, E.V. Ramos-Fernández, R. López-Fonseca, J. Gascon, M. Makkee, J.I. Gutiérrez-Ortiz, Influence of the synthesis route on the catalytic oxidation of 1,2-dichloroethane over CeO₂/H-ZSM5 catalysts, Appl. Catal. A Gen. 456 (2013) 96–104, <https://doi.org/10.1016/j.apcata.2013.02.026>.
- [65] J. Matta, D. Courcot, E. Abi-Aad, A. Aboukaïs, Identification of vanadium oxide species and trapped single electrons in interaction with the CeVO₄ phase in vanadium – cerium oxide systems. 51V MAS NMR, EPR, Raman, and thermal analysis studies, Chem. Mater. 14 (2002) 4118–4125, <https://doi.org/10.1021/cm010396t>.
- [66] M. Defaux, M. Che, C. Naccache, Electron paramagnetic resonance study of oxygen adsorption on supported molybdenum and cerium oxides, Comptes Rendus Acad. Sci. Paris 100 (1969) 2255–2257.
- [67] L.K. Aminov, I.N. Kurkin, R.M. Rakhmatullin, R. Böttcher, A. Pöpli, S. Sen, EPR of Gd³⁺ ion in mixed CeO₂-Y₂O₃ nanocrystals, Phys. Solid State 51 (2009) 2282, <https://doi.org/10.1134/S1063783409110146>.
- [68] H.-F. Wang, H.-Y. Li, X.-Q. Gong, Y.-L. Guo, G.-Z. Lu, P. Hu, Oxygen vacancy formation in CeO₂ and Ce_{1-x}ZrxO₂ solid solutions: electron localization, electrostatic potential and structural relaxation, Phys. Chem. Chem. Phys. 14 (2012) 16521–16535, <https://doi.org/10.1039/C2CP42220D>.
- [69] Q. Dai, S. Bai, X. Wang, G. Lu, Catalytic combustion of chlorobenzene over Ru-doped ceria catalysts: mechanism study, Appl. Catal. B Environ. 129 (2013) 580–588, <https://doi.org/10.1016/j.apcatb.2012.10.006>.
- [70] G. Preda, A. Migani, K.M. Neyman, S.T. Bromley, F. Illas, G. Pachioni, Formation of superoxide anions on ceria nanoparticles by interaction of molecular oxygen with Ce³⁺ sites, J. Phys. Chem. C. 115 (2011) 5817–5822, <https://doi.org/10.1021/jp111147y>.
- [71] S. Karmakar, H.L. Greene, Oxidative destruction of chlorofluorocarbons (CFC11 and CFC12) by zeolite catalysts, J. Catal. 138 (1992) 364–376, [https://doi.org/10.1016/0021-9517\(92\)90029-H](https://doi.org/10.1016/0021-9517(92)90029-H).
- [72] R. López-Fonseca, A. Aranzabal, J.I. Gutiérrez-Ortiz, J.I. Álvarez-Uriarte, J.R. González-Velasco, Comparative study of the oxidative decomposition of trichloroethylene over H-type zeolites under dry and humid conditions, Appl. Catal. B Environ. 30 (2001) 303–313, [https://doi.org/10.1016/S0926-3373\(00\)00244-7](https://doi.org/10.1016/S0926-3373(00)00244-7).
- [73] H.A. Miran, M. Altarawneh, Z.-T. Jiang, H. Oskierski, M. Almatarneh, B.Z. Dlugogorski, Decomposition of selected chlorinated volatile organic compounds by ceria (CeO₂), Catal. Sci. Technol. 7 (2017) 3902–3919, <https://doi.org/10.1039/C7CY01096F>.
- [74] A. Intiso, J. Martínez-Triguero, R. Cuccinello, F. Rossi, A.E. Palomares, Influence of the synthesis method on the catalytic activity of mayenite for the oxidation of gas-phase trichloroethylene, Sci. Rep. 9 (2019) 425, <https://doi.org/10.1038/s41598-018-36708-2>.
- [75] A. Intiso, J. Martínez-Triguero, R. Cuccinello, A. Proto, E.A. Palomares, F. Rossi, A Novel Synthetic Route to Prepare High Surface Area Mayenite Catalyst for TCE Oxidation, Catal. 9 (2019), <https://doi.org/10.3390/catal9010027>.
- [76] A. Davó-Quiñónero, M. Navlani-García, D. Lozano-Castelló, A. Bueno-López, J.A. Anderson, Role of hydroxyl groups in the preferential oxidation of CO over copper oxide-cerium oxide catalysts, ACS Catal. 6 (2016) 1723–1731, <https://doi.org/10.1021/acscatal.5b02741>.
- [77] S. Scirè, S. Minicò, C. Crisafulli, G. Burgio, V. Giuffrida, Catalytic combustion of chlorobenzene over Pt/zeolite catalysts, Appl. Catal. B Environ. Elsevier, 2007, pp. 1023–1030, [https://doi.org/10.1016/s0167-2991\(02\)80259-2](https://doi.org/10.1016/s0167-2991(02)80259-2).
- [78] Q. Dai, S. Bai, Z. Wang, X. Wang, G. Lu, Catalytic combustion of chlorobenzene over Ru-doped ceria catalysts, Appl. Catal. B Environ. 126 (2012) 64–75, <https://doi.org/10.1016/j.apcatb.2012.07.008>.
- [79] N. Phonthammachai, M. Rumruangwong, E. Gulari, A.M. Jamieson, S. Jitkarunka, S. Wongkasemjit, Synthesis and rheological properties of mesoporous nanocrystalline CeO₂ via sol-gel process, Colloids Surf. A Physicochem. Eng. Asp. 247 (2004) 61–68, <https://doi.org/10.1016/j.colsurfa.2004.08.030>.